ADVANCED ENERGY MATERIALS
www.advenergymat.de

Tailoring the Electron and Phonon Transport in Metavalently Bonded GeTe by Stepwise Doping

Ming Liu, Muchun Guo, Yuxuan Yang, Xingyan Dong, Haiyan Lyu, Yingda Lai, Yang Zhang, Yuke Zhu, Hao Wu, Fengkai Guo, Zihang Liu, Wei Cai, Matthias Wuttig, Haijun Wu, Yuan Yu,* and Jiehe Sui**

The intertwining between thermal and electrical transport poses significant challenges to enhancing thermoelectric performance. Chemical doping with a single element often can optimize one of the parameters yet may deteriorate others, restricting the upper limit of *ZT* achievable. Multi-element doping can address this interdependence, allowing for simultaneous optimization of electrical and thermal properties. However, a clear selection rule for multiple dopants remains unclear. Here, a stepwise strategy is shown to improve the thermoelectric performance of metavalently bonded GeTe by enhancing density-of-states effective mass, increasing carrier mobility, and reducing thermal conductivity. These effects are realized by continuously introducing band convergence, lattice plainification, and structural defects. Specifically, band convergence is achieved by Cd doping to reduce the energy offset between light and heavy bands. The lattice plainification is enabled by filling Ge vacancies with Cu, which improves carrier mobility. Lastly, the lattice thermal conductivity is reduced via increasing phonon scattering by point defects caused by Pb doping and nanoprecipitates associated with all these dopants. Consequently, a peak *ZT* of 2.2 at 773 K and an average ZT_{ave} of 1.27 within 300–773 K are realized in $Ge_{0.86}Pb_{0.1}Cd_{0.04}Te$-2%$Cu_2Te$. This work provides a synergistic strategy to modulate electron and phonon transport in metavalently bonded materials.

1. Introduction

Exploiting clean energy technologies is vital to mitigate the energy and environmental crisis.[1] Thermoelectric (TE) materials enable the direct and reversible conversion between thermal energy and electricity, promising applications in waste heat harvesting and distributed cooling.[2] The conversion efficiency of TE materials is mainly determined by the dimensionless figure of merit $ZT = S^2\sigma T/\kappa_{tot}$, where S is the Seebeck coefficient, σ is the electrical conductivity, T is the absolute temperature, and κ_{tot} is the total thermal conductivity (primarily including the electronic (κ_e) and lattice (κ_L) components of the thermal conductivity).[3] Optimizing the charge carrier concentration (n_H) is often the primary step to improve ZT since S and σ are inversely correlated with the carrier density.[4,5,6] Once the n_H is optimum, the ZT value can be further enhanced by tuning the intrinsic physical parameters

M. Liu, X. Dong, Y. Lai, Y. Zhu, H. Wu, F. Guo, Z. Liu, W. Cai, J. Sui
National Key Laboratory for Precision Hot Processing of Metals
Harbin Institute of Technology
Harbin 150001, China
E-mail: suijiehe@hit.edu.cn

M. Liu, H. Lyu, M. Wuttig, Y. Yu
Institute of Physics (IA)
RWTH Aachen University
52074 Aachen, Germany
E-mail: yu@physik.rwth-aachen.de

The ORCID identification number(s) for the author(s) of this article can be found under https://doi.org/10.1002/aenm.202405178

DOI: 10.1002/aenm.202405178

M. Guo
School of Materials Science and Engineering
Xihua University
Chengdu 610039, China

Y. Yang, Y. Zhang, H. Wu
State Key Laboratory for Mechanical Behavior of Materials
Xi'an Jiaotong University
Xi'an 710049, China
E-mail: wuhaijunnavy@xjtu.edu.cn

M. Wuttig
Green IT (PGI 10)
Forschungszentrum Jülich GmbH
52428 Jülich, Germany

of the material, which has been summarized in the so-called B factor,[7,8]

$$B = \left(\frac{k_B}{e}\right)^2 \frac{8\pi e\left(2m_e k_B T\right)^{3/2}}{3h^3} \frac{\mu_W}{\kappa_L} T \propto \left(\frac{m_d^*}{m_e}\right)^{3/2} \frac{\mu_H}{\kappa_L} T \quad (1)$$

where k_B is the Boltzmann constant, h is the Planck constant, μ_w is the weighted mobility, μ_H is the carrier mobility, m_d^* is the density-of-states (DOS) effective mass, and m_e is the electron mass. The larger the B factor, the higher the ZT value achievable.[9] It is clear that enhancing B requires to increase m_d^* and μ_H as well as to reduce κ_L. However, an increased m_d^* leads to reduced μ_H. Methods for lowering κ_L often sacrifice μ_H as well.[10,11–13] Thus, it is a complex and systematic engineering task to improve the ZT value of a given material.

GeTe is a promising p-type thermoelectric material for power generation.[14,15,16] Yet, the low formation energy of Ge vacancies due to the weak metavalent bonds[8,17,18,19] results in high n_H, low μ_H, low S, and high κ_e.[4,6,17,20] The hole concentration can be reduced by introducing aliovalent donor dopants such as Bi and Sb, which has indeed led to an enhancement in the S and power factor ($PF = S^2\sigma$).[6,21–23] However, the μ_H has also been decreased due to the increased point defect scattering for charge carriers.[12,23,24] Moreover, Bi or Sb doping does not change the electronic band structure of GeTe and thus does not affect the m_d^*.[25] In this regard, this kind of doping even degrades the intrinsic electrical properties of GeTe. This can be indicated by the reduced weighted mobility or electronic quality factor upon doping Bi or Sb in GeTe.[22,26] On the contrary, other dopants such as Ta, Mn, Zn, and In can enhance the m_d^* due to the increased valley degeneracy (N_v) or the local DOS 'hump" near the Fermi level.[27,28,29] These dopants not only reduce the hole concentration but also improve the m_d^*. Consequently, a higher PF can be obtained. Nevertheless, carrier mobility is generally decreased due to the presence of extra dopants and impurity scattering.[29,30] This will strongly restrict the upper limit of weighted mobility and thus PF enhancement. In this regard, dopants that can decrease the hole concentration but also simultaneously increase the m_d^*, as well as maintaining or even improving the μ_H would be the best candidates.

On the other hand, even though introducing dopants can suppress the κ_L, the theoretical minimum can only be achieved by properly designing multi-scale structural defects ranging from point defects to precipitates as well as their associated lattice strain.[8,31,32] This is because the phonon spectrum spans a broad range of wavelengths. In the meantime, the decreased κ_L should not be achieved with a tradeoff to the increased scattering of charge carriers. It has been proposed that a coherent interface could be such an ideal microstructure to scatter phonons but not charge carriers.[33] Yet, such a coherent interface in GeTe has only been observed in a few studies.[34] Exploring more candidates that can form coherent nanoprecipitates in GeTe could broaden the space for tuning the overall transport properties.

In this work, a synergistic optimization of the electrical and thermal transport properties in GeTe has been achieved by introducing multiple dopants including Cd, Cu, and Pb. This leads to a high peak ZT and average ZT_{ave}. The enhancement of properties stems from several factors. First, all these dopants reduce the hole concentration of GeTe, approaching the theoretical optimum range. Second, Cd doping decreases the energy offset of the uppermost two valence bands, as schematized in **Figure 1a**, leading to an enhanced N_v and thus an increased m_d^* and S. Third, Cu can fill the Ge vacancies to plainify the lattice, giving rise to an improved μ_H. Fourth, Pb can significantly lower the κ_L due to the large mass and size difference between Pb and Ge, while the μ_H can be maintained due to the increased crystal symmetry. Last but not least, these dopants form nanoprecipitates which are structurally coherent with the GeTe matrix, resulting in a further reduction of the κ_L without sacrificing the μ_H (see a schematic diagram in Figure 1b). These synergistic effects lead to a notable improvement of PF from 6.3 μW cm^{-1} K^{-2} for pristine GeTe to 19.6 μW cm^{-1} K^{-2} for $Ge_{0.86}Pb_{0.1}Cd_{0.04}Te$-2%$Cu_2Te$ at 300 K. Their corresponding κ_L is also decreased from 2.4 to 1.0 W m^{-1} K^{-1} at 300 K. As a consequence, a high ZT of 2.2 at 773 K, an average ZT_{ave} of 1.27 within 300–773 K (Figure 1c,d). This work demonstrates that the electron and phonon transport in GeTe can be stepwise optimized by combining the contrasting yet compensating doping effects of different dopants to simultaneously enable carrier concentration optimization, band convergence, lattice plainification, and coherent nanoprecipitation.

2. Results and Discussion

2.1. Enhanced Density-of-States Effective Mass by Band Convergence

The first parameter that determines the B factor is the DOS effective mass. Cd has been shown to induce the so-called band convergence effect to enhance m_d^* in GeTe.[28,35,36] Pei et al. have found the highest ZT value in 4% Cd-doped GeTe.[35] Thus, we doped the Ge site with 4% Cd to enhance the m_d^* by band convergence as the first step of property optimization. Even though the band convergence effect has been reported, the distribution of Cd in GeTe has not been investigated thoroughly, especially with an atomic-scale resolution. Here, we show that Cd-rich second phases are often absent within the detection limit of X-ray diffraction (XRD) (Figure S1, Supporting Information), which has often mistakenly attributed a higher solubility of Cd to GeTe. In contrast, these precipitates are observed by electron probe microanalyzer (EPMA), as shown in **Figures 2a** and S2 (Supporting Information). To detect the solubility of Cd in the matrix of $Ge_{0.96}Cd_{0.04}Te$, atom probe tomography (APT) characterizations were carried out with ultrahigh chemical sensitivity and spatial resolution.[13,37] The APT reconstruction maps and composition profile show a homogeneous distribution but a low solubility of ≈2% Cd in the matrix (Figure S3a, Supporting Information and the inset of Figure 2b). This also indicates that extra Cd exists in the form of precipitates. The low solubility of Cd in GeTe mainly originates from the difference in chemical bonding mechanisms between GeTe and CdTe.[38] While GeTe employs metavalent bonding as corroborated by the high value of "probability of multiple events" (PME) shown in Figure S3b (Supporting Information) (≈80%), CdTe utilizes covalent bonding and shows a much lower PME value (≈20%).[39,40–42] Aberration-corrected scanning transmission electron microscopy (STEM) was employed to further investigate the second phase and associated interfaces. Nanoprecipitates are observed in the low-magnification high-angle annular dark field (HADDF) image (Figure 2c), which

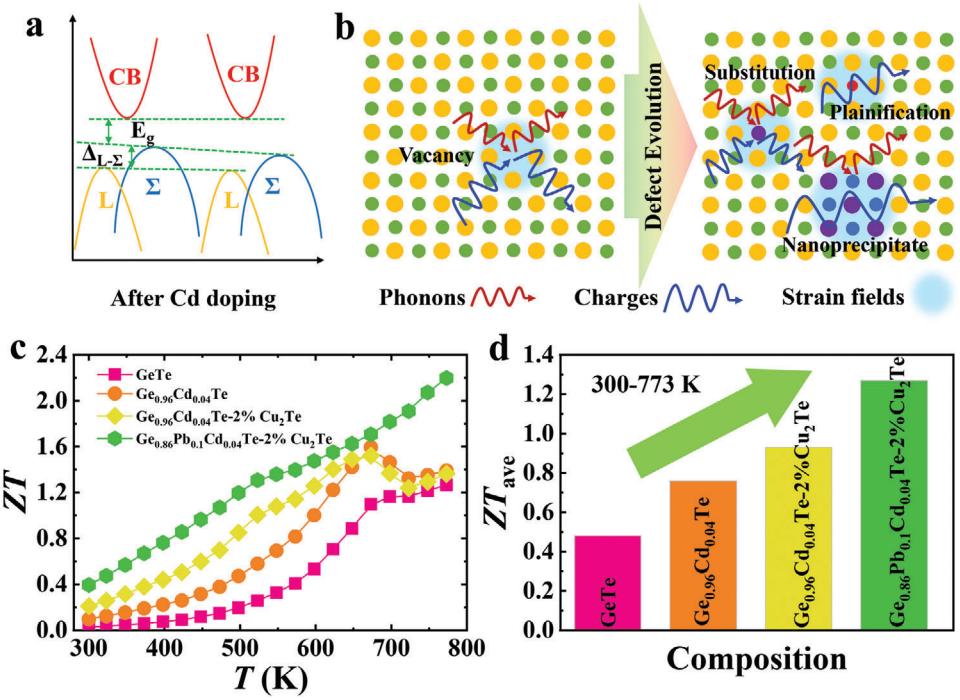

Figure 1. Schematic illustration and thermoelectric performance. a) Schematic band convergence of GeTe by Cd doping; b) Schematic illustration of the effects of point defects, lattice planification, and nanoprecipitates on the transport of electrons and phonons. c) Temperature-dependent ZT and d) average ZT_{ave} comparisons for the GeTe, $Ge_{0.96}Cd_{0.04}Te$, $Ge_{0.96}Cd_{0.04}Te$-2%Cu_2Te, and $Ge_{0.86}Pb_{0.1}Cd_{0.04}Te$-2%$Cu_2Te$ samples.

is consistent with the EMPA results. The interface between the GeTe matrix and the CdTe nanoprecipitate is identified as coherent, as shown in the STEM-HADDF image in Figure 2d. The fast Fourier transformation (FFT) patterns confirm the parallel zone axes of [110] for GeTe and [011] for CdTe, as shown in Figure 2e1 and e 2, respectively. The geometric phase analyses (GPA) for the area in the inset of Figure 2c show large strains at the interface of the matrix and nanoprecipitate (Figure 2f1,f2). Moreover, there are high-density ferroelectric domains in the $Ge_{0.96}Cd_{0.04}Te$ sample (Figure 2g). Despite no dislocations being found in the domain (see the STEM annular bright field (ABF) images in Figure 2h,i), the local distortion and different polarizations lead to a large strain, as demonstrated in the GPA maps along the ε_{xx} (Figure 2j1) and ε_{xy} (Figure 2j2) directions. All these strains provide effective scattering sources for heat-carrying phonons with low and intermediate frequencies.[43]

The effect of Cd doping on the band structure of GeTe can be revealed by first-principles calculations based on density functional theory. **Figures** 3a and S4 (Supporting Information) show that the energy offset between the light and heavy bands is reduced, rendering the enhancement of m_d^* (Table S1, Supporting Information) and thus the increase of S (Figure 3b). It is noteworthy that Cd doping slightly increases the bandgap, which may increase the onset temperature of the bipolar effect. Yet, the bipolar effect is not significant in Cd-doped GeTe due to its high carrier concentration (Table S1, Supporting Information). Therefore, the slightly increased bandgap has no straightforward effects on the thermoelectric performance besides the concomitant band convergence. In addition, the decrease in the Seebeck coefficient with increasing temperature is due to phase transition rather than bipolar effect.[28,35] However, Cd doping significantly decreases μ_H (Table S1, Supporting Information) due to the strengthening of carrier-ionized impurity scattering. The electrical conductivity decreases upon Cd doping because of the decrease in both n_H and μ_H (Figure S5a, Supporting Information). Note that the improvement of S is mainly induced by the enlarged m_d^* due to the band convergence effect, while the reduced n_H is an additional effect, as can be reflected by the Pisarenko plot in Figure 3c. Thanks to the significantly enhanced S, the PF increases from 6.3 μW cm^{-1} K^{-2} for the pristine GeTe to 12.8 μW cm^{-1} K^{-2} for the $Ge_{0.96}Cd_{0.04}Te$ sample at 300 K (Figure S5b, Supporting Information). The reduction of κ_{tot} in Cd-doped GeTe roots in the suppression of both κ_e and κ_L (Figure S6, Supporting Information). Because of the decrease of σ, κ_e is also reduced ($\kappa_e = L\sigma T$, where L is the Lorenz factor calculated by a single parabolic band model with acoustic phonon scattering[44]). The suppression of κ_L comes from the joint effects of the strengthened phonon scattering across a broad frequency range by point defects and CdTe nanoprecipitates (NP_1). Finally, due to the versatile effects of Cd doping, the ZT is improved in the $Ge_{0.96}Cd_{0.04}Te$ sample in the whole temperature range measured (Figure 3d).

2.2. Improved Carrier Mobility by Lattice Plainification

Even though Cd doping can enhance the power factor and ZT value of GeTe, unfortunately, the Hall mobility is also significantly reduced. This to some extent underscores the effect of Cd doping. Thus, an additional element should be introduced to restore the Hall mobility. It has been demonstrated in many

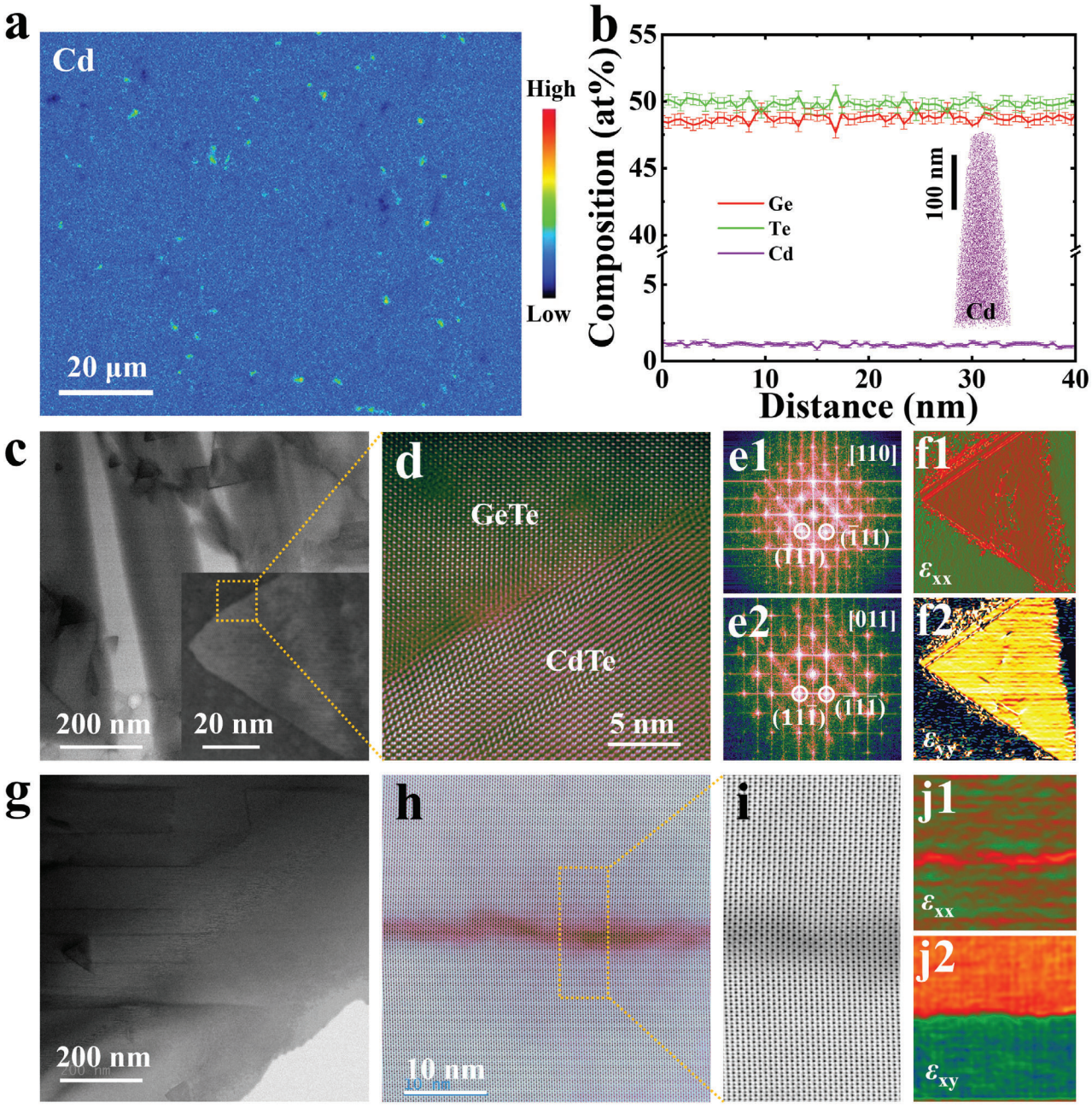

Figure 2. Microstructure of $Ge_{0.96}Cd_{0.04}Te$ sample. a) EPMA mapping of Cd in the $Ge_{0.96}Cd_{0.04}Te$ sample; b) Composition profile of elements taken from a cuboid region of interest along the vertical direction for $Ge_{0.96}Cd_{0.04}Te$ sample measured by atom probe tomography. The inset shows the 3D distribution of Cd in the matrix; c) Low-magnification STEM image for the $Ge_{0.96}Cd_{0.04}Te$ sample, and the inset shows the high-magnification HADDF image highlighting the faceted precipitate; d) Atomically-resolved STEM-HAADF image showing the interface between the matrix and precipitate taken from the yellow square of the inset of (c); e1-e2) Fast Fourier transformation (FFT) patterns of the GeTe matrix and the CdTe precipitate; f1-f2) GPA strain maps for the area in inset of Figure 2c along ε_{xx} and ε_{yy}; g) STEM-HAADF image showing the ferroelectric domains; h) STEM-ABF image showing the atomic structures of the domain; i) A close-up near the domain area as indicated by a yellow rectangle in h; j1-j2) GPA strain maps for the area shown in Figure 2h along the ε_{xx} and ε_{xy} directions.

IV–VI chalcogenides that introducing Cu can enhance overall carrier mobility. Therefore, Cu_2Te is utilized to alloy with GeTe. The increase of lattice parameters and interaxial angles (Figure S7, Supporting Information) implies that Cu enters into the lattice. Similar to the case of Cd doping in GeTe, Cu_2Te also suffers from the issue of low solid solubility limit in GeTe. XRD results indicate a solubility lower than 2% because the lattice parameters and interaxial angles saturate above this content. EPMA results show CuCd-rich precipitates (NP_2) in the $Ge_{0.96}Cd_{0.04}Te$-2%Cu_2Te sample in addition to the Cd-rich precipitates, as shown

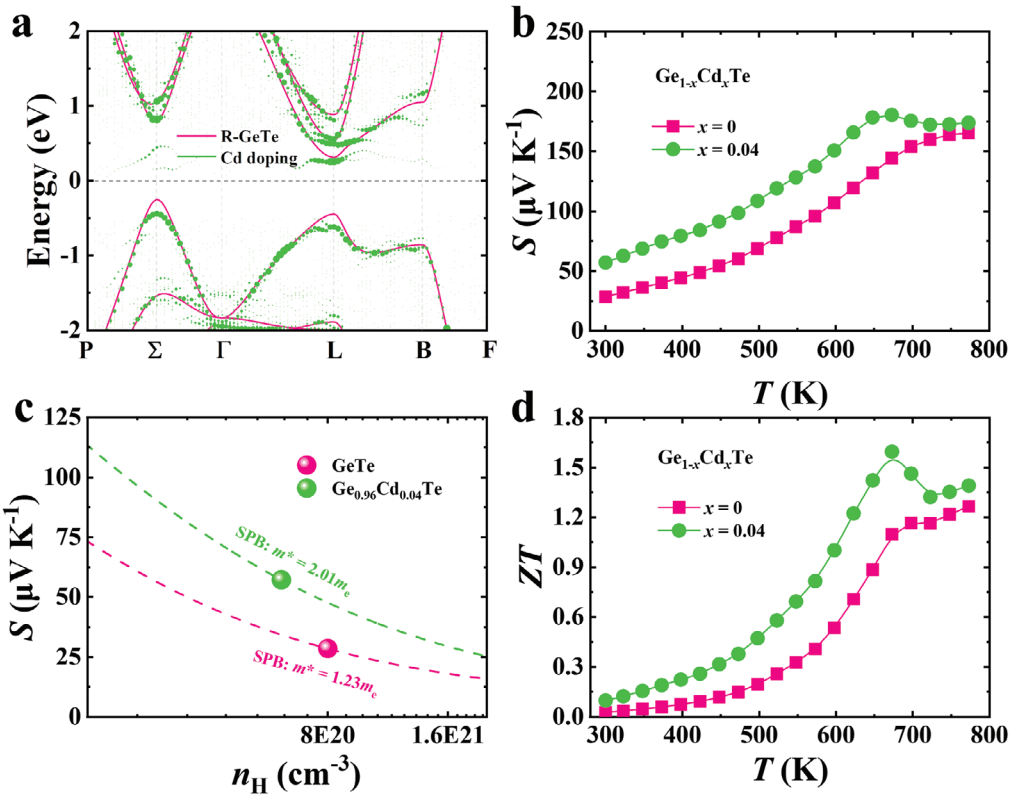

Figure 3. Band structure and thermoelectric performance of $Ge_{0.96}Cd_{0.04}Te$ sample. a) Band structures for pristine R-GeTe and Cd-doped GeTe; b) The *S* for GeTe and $Ge_{0.96}Cd_{0.04}Te$ samples; c) Room-temperature *S* as a function of the carrier concentration for GeTe and $Ge_{0.96}Cd_{0.04}Te$ samples; d) *ZT* values for GeTe and $Ge_{0.96}Cd_{0.04}Te$ samples.

in **Figures** 4a and S8 (Supporting Information). More quantitative analysis by APT reveals that the solubility of Cu slightly exceeds 1% in the matrix of $Ge_{0.96}Cd_{0.04}Te$-2%Cu_2Te (Figure 4b). The dissolved Cu atoms show a uniform distribution in the matrix, as illustrated in Figure S9 (Supporting Information). The size of precipitates is in the nanoscale, as demonstrated in Figure S10 (Supporting Information). Interestingly, there is only a single set of diffraction patterns within the area including both the matrix and the CuCd-rich nanoprecipitate, as shown in Figure 4c and its inset. This indicates a perfect coherent lattice structure of the precipitate with the matrix. We even observed a domain structure in the CuCd-rich precipitate as shown in Figure 4d, which is typically observed in rhombohedral GeTe. Large strain still exists in the phase boundary and domain boundary (Figure 4e), which is favorable for scattering phonons. This kind of coherent atomic arrangement between the CuCd-rich precipitate and the GeTe matrix is found randomly in the sample, as displayed by the STEM-HADDF image in Figure 4f. Obviously, the co-enrichment of Cu and Cd changes the atomic structures of the precipitate, which is different from the binary CdTe. This second phase has also been detected in APT characterizations. A Cd/Cu-rich while Ge-poor area can be observed in the 3D reconstruction maps of $Ge_{0.96}Cd_{0.04}Te$-2%Cu_2Te in Figure 4g. The 1D composition profile across the interface between the precipitate and matrix shows that the cations in the CuCd-rich precipitate include Cu, Cd, and Ge with a total composition of 50%, while the matrix is GeTe with a low content of soluble Cd and Cu (Figure 4h). It appears that the CuCd-rich precipitates are formed by the clustering of Cu and Cd in GeTe which still utilize the GeTe lattice, as identified by STEM. Meanwhile, the PME value of the CuCd-rich precipitate is lower than that of the matrix, as shown in Figure 4i. A large number of Cu and Cd occupying Ge sites could change the values for electron transfer and electron sharing and thus modify the chemical bonds.[18,32] Nevertheless, the PME value for the second phase is still above 60%, which is typically found in metavalently bonded materials.[40,45] This is indicative of the same bonding mechanism for the GeTe matrix and the CuCd-rich precipitate. Given the coherent structure and the same bonding mechanism across the interface, it is plausible that this precipitate will not seriously decrease the electrical properties. Yet, the strains can lower the thermal conductivity.

We then performed aberration-corrected STEM characterizations to determine the position of Cu atoms in the $Ge_{0.96}Cd_{0.04}Te$-2%Cu_2Te matrix. **Figure** 5a shows the atomically-resolved STEM-HAADF image along the [110] zone axis of $Ge_{0.96}Cd_{0.04}Te$. The Ge and Te atomic columns can be clearly distinguished along this viewing direction, where Ge atoms are smaller and lighter while Te atoms are bigger and brighter. Figure 5b displays the intensity mapping of the Ge sites relative to the surrounding Te sites of the $Ge_{0.96}Cd_{0.04}Te$ (Figure 5a) sample based on the quantitative analysis of the individual atomic columns of the atomically-resolved STEM-HAADF image. The calculation method is to divide the intensity β of Ge sites by the average intensity δ of the four surrounding Te atoms to obtain a numerical value γ.

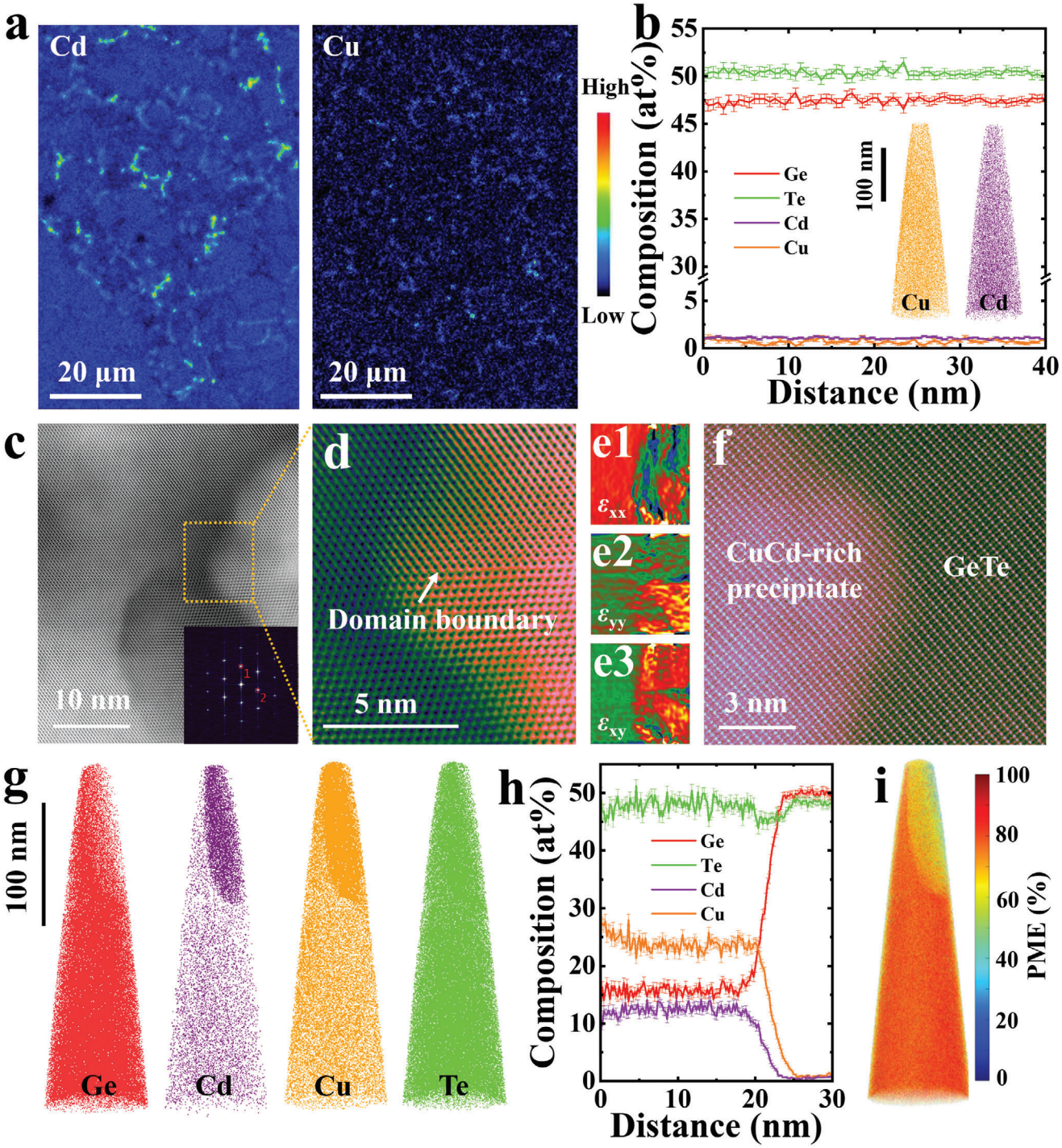

Figure 4. Microstructure of $Ge_{0.96}Cd_{0.04}Te$-2%Cu_2Te sample. a) EPMA mapping of Cd and Cu for $Ge_{0.96}Cd_{0.04}Te$-2%Cu_2Te sample; b) Composition profile of elements taken from a cuboid region of interest along the vertical direction for $Ge_{0.96}Cd_{0.04}Te$-2%Cu_2Te sample. Inset shows the 3D distribution of Cu and Cd in the matrix; c) STEM-ABF image shows the interface between the second phase and the matrix in $Ge_{0.96}Cd_{0.04}Te$-2%Cu_2Te, and the inset shows the selected area electron diffraction (SAED) pattern; d) A close-up of the interface indicated by a frame in (c); e1–e3) GPA strain maps for the area shown in (d) along the ε_{xx}, ε_{yy} and ε_{xy} directions; f) Atomically-resolved STEM-HAADF image showing the interface between second phase and matrix in the $Ge_{0.96}Cd_{0.04}Te$-2%Cu_2Te sample; g) 3D distribution of elements for $Ge_{0.96}Cd_{0.04}Te$-2%Cu_2Te sample; h) Composition profile of elements taken from a cuboid region of interest along the direction perpendicular to the interface between the matrix and the second phase for $Ge_{0.96}Cd_{0.04}Te$-2%Cu_2Te sample; i) 3D PME map for $Ge_{0.96}Cd_{0.04}Te$-2%Cu_2Te sample.

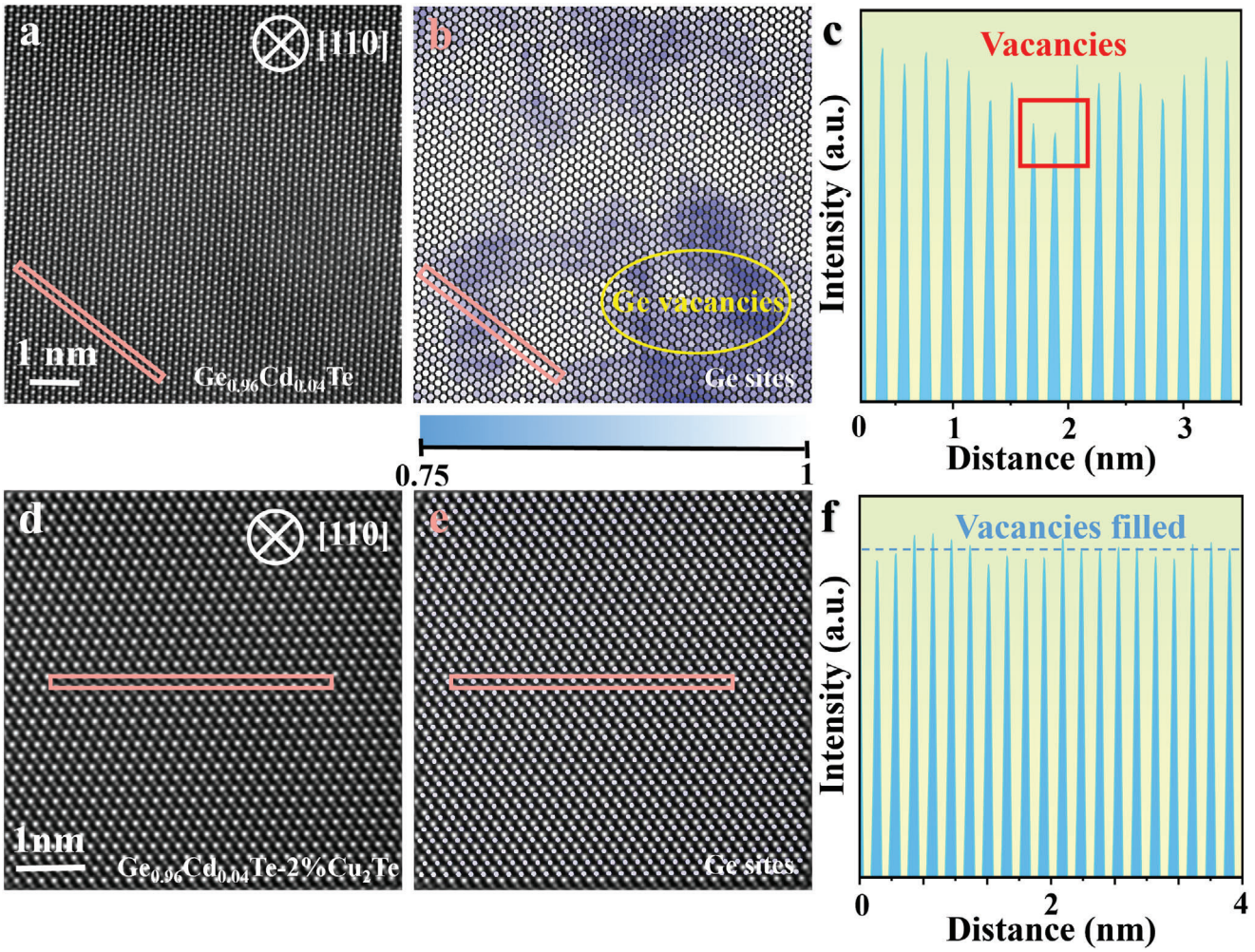

Figure 5. Comparison of the microstructure of $Ge_{0.96}Cd_{0.04}Te$ and $Ge_{0.96}Cd_{0.04}Te$-2%Cu_2Te samples at the atomic scale. Atomically-resolved STEM HAADF images along the [110] zone axes of (a) $Ge_{0.96}Cd_{0.04}Te$ and d $Ge_{0.96}Cd_{0.04}Te$-2%Cu_2Te samples; b,e) Intensity mapping of the Ge sites relative to the surrounding Te atoms of a $Ge_{0.96}Cd_{0.04}Te$ and d) $Ge_{0.96}Cd_{0.04}Te$-2%Cu_2Te samples respectively to eliminate the effect of the sample thickness; c, f) Atomic intensity profile for the pink square in (a) and (d), respectively.

And then, Figure 5b is plotted using the ratio of β to the maximum value of γ (γ_{max}), in order to eliminate the effect of the sample thickness. Among them, blue and white points represent lighter/fewer and heavy/more atoms, respectively. Thus, the atomic columns that contain a large fraction of vacancies will show a blue contrast. This has been observed in the $Ge_{0.96}Cd_{0.04}Te$ sample in Figure 5b, providing solid evidence of a high number density of Ge vacancies. The decreased intensity due to the presence of Ge vacancies can also be visualized in a linear intensity profile scanned along the pink square indicated, as shown in Figure 5c. In contrast, a similar analysis for the sample $Ge_{0.96}Cd_{0.04}Te$-2%Cu_2Te shows distinctively different phenomena. Figure 5d shows the atomically-resolved micrograph along the same [110] zone axis. Its corresponding Ge intensity map in Figure 5e does not present noticeable Ge vacancies. The intensity line profile in Figure 5f also implies that the Ge vacancies have been filled by Cu atoms. This will lead to the reduction of n_H and the enhancement of μ_H as proved by Hall measurements shown below. Note that we cannot exclude the existence of interstitial Cu atoms in $Ge_{0.96}Cd_{0.04}Te$-2%Cu_2Te despite their absence in STEM images. Indeed, the existence form of Cu in GeTe depends on the dopants. For example, Cu exists in the interstitial positions in Ti and Bi co-doped GeTe,[16] while Cu forms "vacancy/Cu-Cu/vacancy" sandwich-like stacking faults in Sb-doped GeTe.[15]

Figure 6a shows the n_H and μ_H of $Ge_{0.96}Cd_{0.04}Te$-y%Cu_2Te samples. The n_H decreases while the μ_H increases with increasing the content of Cu_2Te until 2% due to the lattice plainification effect by Cu filling into Ge vacancies as proved in Figure 5. Both n_H and μ_H values are saturated above 2% due to the solid solubility limit, which is consistent with the microstructure characterizations. Figure 6b shows that the carrier mobility of $Ge_{0.96}Cd_{0.04}Te$-y%Cu_2Te samples is higher than that of other reported results at the same carrier concentration due to the reduced scattering effect of vacancies on carriers.[4] Figure 6c displays the temperature-dependent weighted mobility μW, which is an indicator of the electrical transport performance independent of doping level, calculated using experimental electrical conductivity σ

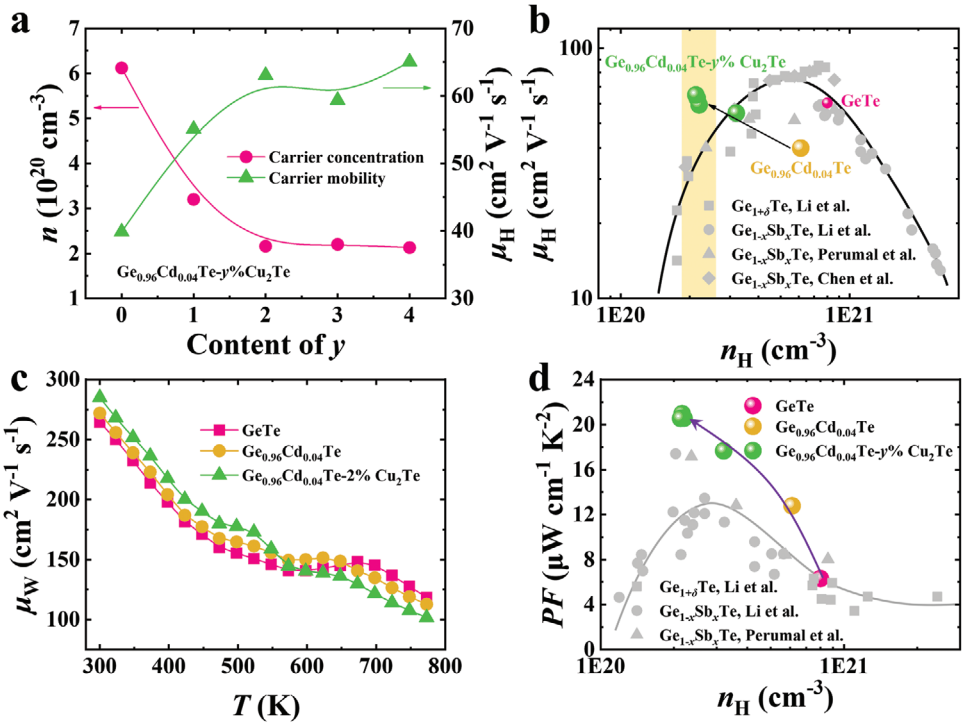

Figure 6. Electrical transport performance of $Ge_{0.86}Cd_{0.04}Te$-2%Cu_2Te sample. a) Carrier concentration and mobility for $Ge_{0.96}Cd_{0.04}Te$-y%Cu_2Te samples; b) Room-temperature carrier concentration as a function of the carrier mobility for GeTe, $Ge_{0.96}Cd_{0.04}Te$, $Ge_{0.96}Cd_{0.04}Te$-y%Cu_2Te and references[6,21,25,49]; c) Temperature-dependent weighted mobility for GeTe, $Ge_{0.96}Cd_{0.04}Te$, $Ge_{0.96}Cd_{0.04}Te$-2%Cu_2Te samples; d) Room-temperature *PF* as a function of carrier concentration for GeTe, $Ge_{0.96}Cd_{0.04}Te$, $Ge_{0.96}Cd_{0.04}Te$-2%Cu_2Te and references.[6,21,25]

and Seebeck coefficient *S* following the Equation (2) proposed by Snyder et al.[46]

$$\mu_W = \frac{3h^3\sigma}{8\pi e(2m_e k_B T)^{3/2}} \left[\frac{\exp\left[\frac{|S|}{k_B/e} - 2\right]}{1+\exp\left[-5\left(\frac{|S|}{k_B/e}-1\right)\right]} + \frac{\frac{3}{\pi^2}\frac{|S|}{k_B/e}}{1+\exp\left[5\left(\frac{|S|}{k_B/e}-1\right)\right]} \right] \quad (2)$$

The enhancement of μW for $Ge_{0.96}Cd_{0.04}Te$ compared to pristine GeTe below the phase transition temperature proves the positive effect of Cd on modifying the band structure. Yet, this enhancement is still marginal due to the tradeoff between DOS effective mass and carrier mobility. In contrast, the introduction of Cu to fill Ge vacancies in $Ge_{0.96}Cd_{0.04}Te$-2%Cu_2Te causes a prominent enhancement of the weighted mobility. The μW increases from 265 $cm^2V^{-1}s^{-1}$ for GeTe to 285 $cm^2V^{-1}s^{-1}$ for $Ge_{0.96}Cd_{0.04}Te$-2%Cu_2Te at room temperature. The filling of Ge vacancies by Cu can also lead to a significant reduction of n_H, giving rise to the decrease in σ and increase in *S* below the phase transition temperature of GeTe (See the thermoelectric properties of $Ge_{0.96}Cd_{0.04}Te$-y%Cu_2Te samples in Figure S11, Supporting Information). The reason for the unchanged σ and *S* above the phase transition temperature could be ascribed to the increased Ge vacancies due to the lower formation energy of a Ge vacancy in the cubic phase.[47] The high content of Ge vacancies generates a much larger hole carrier density, which overwhelms the effect of Cu doping on the TE properties of GeTe. A similar phenomenon has also been observed in other studies about Cu doping in GeTe.[15,16] Meanwhile, the m_d^* slightly reduces after Cu_2Te alloying (Figure S12, Supporting Information), which is attributed to the decrease of Ge vacancies. Decreasing Ge vacancies can separate different valence bands of GeTe.[4,48] Figure 6d shows a maximum *PF* of 21.0 μW cm^{-1} K^{-2} at 300 K in the $Ge_{0.96}Cd_{0.04}Te$-2%Cu_2Te sample, which is much higher than other GeTe-based materials at the same carrier concentrations. This indicates the significant benefit of improved μ_H to the electrical properties realized by lattice plainification. The reduction of κ_{tot} (Figure S11d, Supporting Information) after Cu_2Te alloying primarily originates from the significantly decreased κ_e by the reduced σ. In contrast, the κ_L is barely changed (Figure S11e, Supporting Information) due to the compromise of the strengthened nanoprecipitate scattering by CuCd-rich nanoprecipitates and the weakened point defect (Ge vacancies) scattering by lattice plainification. These factors lead to an enhancement of *ZT* below the phase transition temperature in the $Ge_{0.96}Cd_{0.04}Te$-y%Cu_2Te samples (Figure S11f, Supporting Information).

2.3. Reduced Lattice Thermal Conductivity by Nanoprecipitation and Point Defects

Note that the κ_L obtained so far is still much higher than the theoretical minimum of GeTe (0.45 W m^{-1} K^{-2}, calculated by the Cahill model[50,51]). This implies that further *ZT* improvement can be achieved if the κ_L can be reduced. Pb element

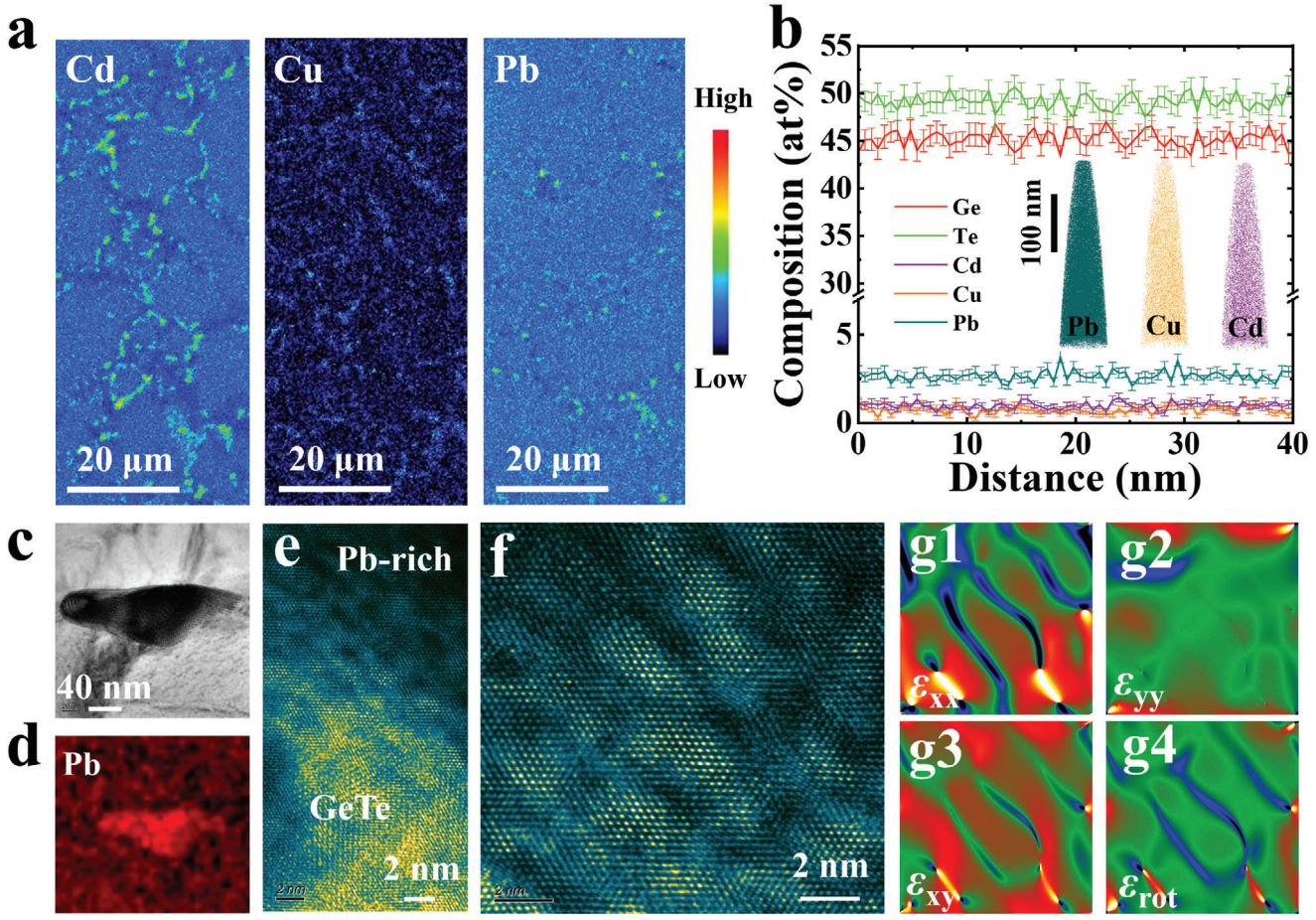

Figure 7. Microstructure of $Ge_{0.86}Pb_{0.1}Cd_{0.04}Te$-2%$Cu_2Te$ sample. a) EPMA mapping of Cd, Cu, and Pb for the $Ge_{0.86}Pb_{0.1}Cd_{0.04}Te$-2%$Cu_2Te$ sample; b) Composition profile of elements taken from a cuboid region of interest along the vertical direction for the $Ge_{0.86}Pb_{0.1}Cd_{0.04}Te$-2%$Cu_2Te$ sample; c) TEM image of the second phase and matrix for the $Ge_{0.86}Pb_{0.1}Cd_{0.04}Te$-2%$Cu_2Te$ sample; d) TEM-EDS showing the Pb-rich second phase; e) The interface between the Pb-rich precipitate and the matrix of $Ge_{0.86}Pb_{0.1}Cd_{0.04}Te$-2%$Cu_2Te$; f) Enlarged view of the Pb-rich second phase, where the fluctuation of composition as indicated by different intensity contrasts is due to spinodal decomposition of GeTe-PbTe; g1–g4) GPA strain maps along the ε_{xx}, ε_{yy}, ε_{xy}, and ε_{rot} directions for the corresponding area of (f).

has been proven to be an effective dopant for reducing κ_L in GeTe.[22,52] Therefore, we further introduce Pb doping to reduce the κ_L. XRD patterns show that the additional diffraction peaks indicated by arrows can be indexed to PbTe (Figure S13, Supporting Information). EPMA results (**Figure** 7a; Figure S14, Supporting Information) also show Pb-rich precipitates (NP_3) in the $Ge_{0.86}Pb_{0.1}Cd_{0.04}Te$-2%$Cu_2Te$ sample. According to the literature,[52] the solubility of Pb in GeTe is ≈5%. Thus, it is reasonable to observe the PbTe phase in our sample with a nominal Pb content of 10%. Based on the APT results (Figure 7b), ≈5% Pb (corresponding to 2.5 at% in the APT composition profile) can dissolve into the matrix of $Ge_{0.86}Pb_{0.1}Cd_{0.04}Te$-2%$Cu_2Te$. All these dopants including Pb, Cd, and Cu distribute homogeneously in the matrix of $Ge_{0.86}Pb_{0.1}Cd_{0.04}Te$-2%$Cu_2Te$ (see the inset of Figure 7b; Figure S15, Supporting Information). Figure 7c,d show that the precipitate is in nanoscale and Pb-rich. The interface between the Pb-rich precipitate and the matrix of $Ge_{0.86}Pb_{0.1}Cd_{0.04}Te$-2%$Cu_2Te$ is also coherent, as shown in Figure 7e. A high-resolution image taken from the interior of the PbTe-rich precipitate shows strip-like structures (Figure 7f), which could be formed by the spinodal decomposition of a GeTe-PbTe system.[53] These strip-shaped nanostructures induce large strains, as proven by GPA maps in Figure 7g. This can disturb the phonon transport and reduce κ_L.

From the perspective of chemical bonding, both GeTe and PbTe tend to form cubic structures because of their orthogonal alignment of p-orbitals.[42] However, the cubic configuration of GeTe is energetically unstable and undergoes a Peierls distortion, transforming into a rhombohedral structure.[54] Increasing the number of electrons transferred tends to stabilize the cubic structure of the material. According to the chemical bond classification map,[41] PbTe has a higher number of electrons transferred compared to GeTe. Therefore, Pb doping will increase the number of electrons transferred in the material, thereby enhancing its symmetry. It has been demonstrated that doping Pb into GeTe can lower the formation energy of cation vacancies due to the reduced difference in the size between cations and anions.[51] This will result in a reduction in n_H as observed in Figure S16 (Supporting Information). Although the increased alloy scattering will reduce the μ_H (Figure S16, Supporting Information), the

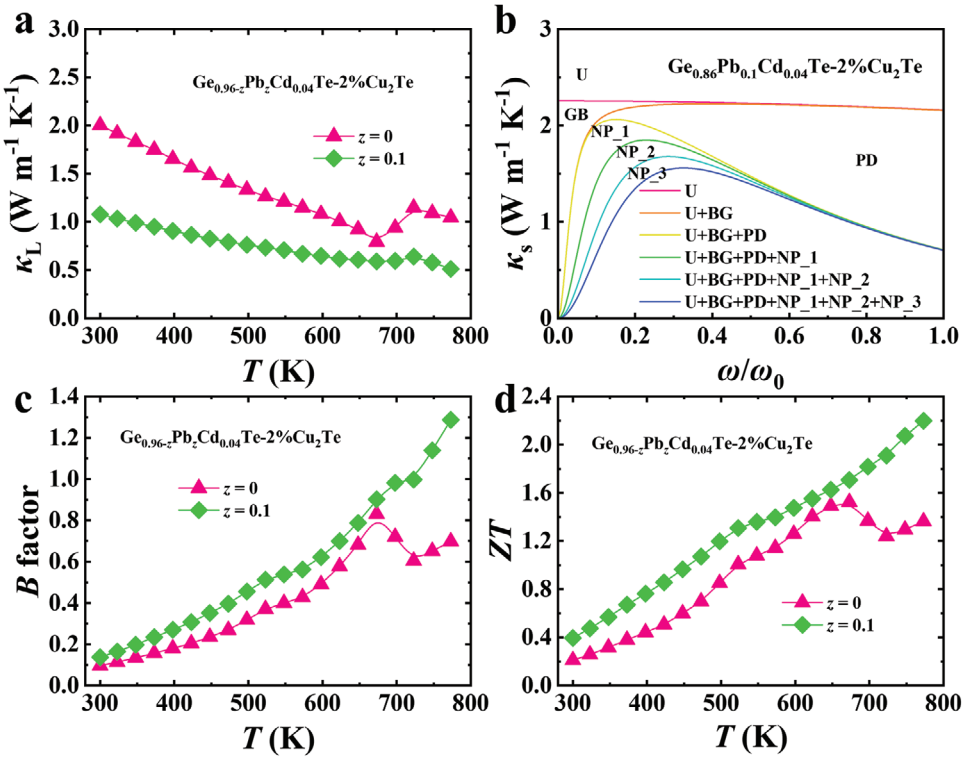

Figure 8. Thermoelectric performance of $Ge_{0.86}Pb_{0.1}Cd_{0.04}Te$-2%$Cu_2Te$ sample. a) The κ_L for $Ge_{0.96}Cd_{0.04}Te$-2%Cu_2Te and $Ge_{0.86}Pb_{0.1}Cd_{0.04}Te$-2%$Cu_2Te$ samples; b) Frequency-dependent κ_L for the $Ge_{0.86}Pb_{0.1}Cd_{0.04}Te$-2%$Cu_2Te$ sample at 300 K; c) *B* factor for $Ge_{0.96}Cd_{0.04}Te$-2%Cu_2Te and $Ge_{0.86}Pb_{0.1}Cd_{0.04}Te$-2%$Cu_2Te$ samples; d) *ZT* value for $Ge_{0.96}Cd_{0.04}Te$-2%Cu_2Te and $Ge_{0.86}Pb_{0.1}Cd_{0.04}Te$-2%$Cu_2Te$ samples.

increase of crystal symmetry after Pb doping is conducive to carrier transport.[11,52] Thus, the μ_H only slightly reduces. Due to the reduction of both n_H and μ_H, the σ is reduced after Pb doping (Figure S17a, Supporting Information), leading to a degradation of the *PF* even though the *S* is increased with n_H reducing (Figure S17b, Supporting Information). Nevertheless, the significant reduction of κ_{tot} (Figure S17d, Supporting Information) contributed by the decrease of κ_e and κ_L can compensate for the decreased electrical properties. Particularly, a prominent decrease in κ_L is achieved over the entire measurement temperature range due to the phonon scattering by point defects and nanoprecipitates, as presented in **Figures** 8a and S17e (Supporting Information). At high temperatures, the mean free path of phonons is comparable to the size of point defects. Based on the APT results, the solid solubility of Pb in GeTe is ≈5%, which introduces significant mass and strain fluctuations to scatter phonons at high temperatures. In addition, STEM reveals that Pb doping introduces nano-precipitates that are coherent with the matrix, causing significant interfacial strain. These collective defects induced by doping Pb can strongly scatter phonons, resulting in a distinct reduction in lattice thermal conductivity. The frequency-dependent κ_s for $Ge_{0.86}Pb_{0.1}Cd_{0.04}Te$-2%$Cu_2Te$ in Figure 8b further quantifies the contribution of each nanoprecipitate and point defects to the accumulative reduction in κ_L. Benefiting from the distinct reduction in κ_L, the *B* factor of $Ge_{0.86}Pb_{0.1}Cd_{0.04}Te$-2%$Cu_2Te$ is significantly increased compared to $Ge_{0.96}Cd_{0.04}Te$-2%Cu_2Te, especially at high-temperature range, as presented in Figure 8c. Here, the relative comparison of the *B* factor is reliable since no bipolar effects occur in $Ge_{0.96}Cd_{0.04}Te$-2%Cu_2Te and $Ge_{0.86}Pb_{0.1}Cd_{0.04}Te$-2%$Cu_2Te$ samples due to their high carrier concentration. The absence of the bipolar effect can be evidenced by the reduced lattice thermal conductivity with increasing temperature (Figure 8a). Note that the upturn of lattice thermal conductivity in the $z = 0$ sample is due to the phase transition from rhombohedral to cubic, rather than the bipolar effect. Ultimately, due to the significantly reduced κ_L by Pb doping, the peak *ZT* of 2.2 at 773 K is achieved in the $Ge_{0.86}Pb_{0.1}Cd_{0.04}Te$-2%$Cu_2Te$ sample (Figure 8d; Figure S17f, Supporting Information). This high *ZT* value has been realized by stepwise introducing various dopants to tailor the microstructures and thus the transport of electrons and phonons.

3. Conclusion

In this work, we have demonstrated that the TE performance of GeTe can be notably enhanced by synergistically introducing band convergence, lattice plainification, nanoprecipitates, and point defects. The band convergence was enabled by the reduced energy offset between the uppermost light and heavy bands by doping Cd, leading to an enhanced density-of-states effective mass and Seebeck coefficient. Alloying the Cd-doped GeTe with Cu_2Te can plainify the lattice by filling the vacancies with Cu, leading to a decreased n_H and increased μ_H. After that, Pb was introduced into the system, resulting in a continuous reduction in n_H without significantly changing μ_H. Benefiting from these effects, a significantly improved *PF* of 19.6 μW cm^{-1} K^{-2} at 300 K

was realized in the $Ge_{0.86}Pb_{0.1}Cd_{0.04}Te$-2%$Cu_2Te$ sample. These dopants such as Cd, Cu, and Pb not only introduce point defects but also induce coherent nanoprecipitates in GeTe. As a result, the heat-carrying phonons can be scattered over a broad frequency range, giving rise to a low κ_L of 0.5 W m^{-1} K^{-2} approaching the amorphous limit. Finally, a peak ZT of 2.2 at 773 K and a high average ZT_{ave} of 1.27 within 300–773 K were obtained in the $Ge_{0.86}Pb_{0.1}Cd_{0.04}Te$-2%$Cu_2Te$ sample. This work suggests a feasible strategy for improving the TE performance of GeTe by stepwise introducing multiple dopants to create a synergistic effect, offering insights into the microstructure and property design in other semiconductors.

Supporting Information

Supporting Information is available from the Wiley Online Library or from the author.

Acknowledgements

This work was supported by the National Natural Science Foundation of China (Nos. 52271206, U23A20556, 524B2021, 52130106, 52101247, and 523B2020), the Fundamental Research Funds for the Central Universities (HIT.DZJJ.2024003), the Natural Science Foundation of Sichuan Province (No. 2024NSFSC0992), the National Key R&D Program of China (2021YFB3201100), and the Xihua University Science and Technology Innovation Competition Project for Postgraduate Students (RC2400002144). The authors thank Mr. Chuansheng Ma from the Instrument Analysis Center of Xi'an Jiaotong University for the assistance of aberration-corrected STEM.

Open access funding enabled and organized by Projekt DEAL.

Conflict of Interest

The authors declare no conflict of interest.

Author Contributions

M.L., M.G., and Y.Y., contributed equally to this work. M.L., Y.Yu., and J.S. developed the concept and designed the experiments. M.G. carried out the theoretical calculations. Y.Yang., M.L., Y.Z., and Haijun.W. conducted aberration-corrected STEM experiments. M.L., H.L., and M.W carried out the APT measurements. M.L., M.G., X.D., Y.L., Y.Z., Hao.W., F.G., Z.L., and W.C. performed the sample preparations and thermoelectric properties measurements. Y.Yu. Haijun.W. and J.S. supervised the whole project. M.L. and Y.Yu. wrote the draft. All authors discussed the results and commented on the manuscript.

Data Availability Statement

The data that support the findings of this study are available from the corresponding author upon reasonable request.

Keywords

band convergence, coherent nanoprecipitates, lattice plainification, metavalent bonding, thermoelectrics

Received: November 5, 2024
Revised: January 3, 2025
Published online: January 16, 2025

[1] S. Zhang, Z. Wu, Z. Liu, Z. Hu, *Adv. Energy Mater.* **2023**, *13*, 2300260.
[2] a) L. E. Bell, *Science* **2008**, *321*, 1457; b) X.-L. Shi, J. Zou, Z.-G. Chen, *Chem. Rev.* **2020**, *120*, 7399; c) D. Luo, Y. Yu, Y. Yan, W.-H. Chen, B. Cao, *Device* **2024**, *2*, 100435.
[3] a) G. J. Snyder, E. S. Toberer, *Nat. Mater.* **2008**, *7*, 105; b) J. He, T. M. Tritt, *Science* **2017**, *357*, eaak9997
[4] M. Liu, Y. Sun, J. Zhu, C. Li, F. Guo, Z. Liu, M. Guo, Y. Zhu, X. Dong, Z. Ge, Q. Zhang, W. Cai, J. Sui, *Acta. Mater.* **2023**, *244*, 118565.
[5] a) Y. Qin, B. Qin, T. Hong, X. Zhang, D. Wang, D. Liu, Z.-Y. Wang, L. Su, S. Wang, X. Gao, Z.-H. Ge, L.-D. Zhao, *Science* **2024**, *383*, 1204; b) T. Xing, C. Zhu, Q. Song, H. Huang, J. Xiao, D. Ren, M. Shi, P. Qiu, X. Shi, F. Xu, L. Chen, *Adv. Mater.* **2021**, *33*, 2008773; c) M. Liu, M. Guo, J. Zhu, X. Zeng, H. Chen, D. Yuan, Q. Zhang, F. Cai, F. Guo, Y. Zhu, X. Dong, W. Cai, Y. Zhang, Y. Yu, J. Sui, *Adv. Funct. Mater.* **2024**, *34*, 2316075.
[6] J. Li, Z. Chen, X. Zhang, Y. Sun, J. Yang, Y. Pei, *NPG Asia Mater.* **2017**, *9*, e353.
[7] a) J. Goldsmid, *Introduction to Thermoelectricity*, Springer, Luxembourg, USA, **2009**; b) J. Shuai, H. Geng, Y. Lan, Z. Zhu, C. Wang, Z. Liu, J. Bao, C.-W. Chu, J. Sui, Z. Ren, *Proc. Natl. Acad. Sci. USA* **2016**, *113*, E4125; c) Y. Pei, H. Wang, G. J. Snyder, *Adv. Mater.* **2012**, *24*, 6125.
[8] Y. Yu, A. Sheskin, Z. Wang, A. Uzhansky, Y. Natanzon, M. Dawod, L. Abdellaoui, T. Schwarz, C. Scheu, M. Wuttig, O. Cojocaru-Mirédin, Y. Amouyal, S. Zhang, *Adv. Energy Mater.* **2024**, *14*, 2304442.
[9] Z. Ren, Y. Lan, Q. Zhang, *Advanced Thermoelectrics: Materials, Contacts, Devices, and Systems*, CRC Press, Boca Raton, Florida, **2018**.
[10] a) Y. K. Zhu, Y. Sun, J. Zhu, K. Song, Z. Liu, M. Liu, M. Guo, X. Dong, F. Guo, X. Tan, B. Yu, W. Cai, J. Jiang, J. Sui, *Small* **2022**, *18*, 2201352; b) F. Guo, M. Liu, J. Zhu, Z. Liu, Y. Zhu, M. Guo, X. Dong, Q. Zhang, Y. Zhang, W. Cai, J. Sui, *Mater. Today Phys.* **2022**, *27*, 100780; c) V. K. Ranganayakulu, T.-H. Wang, C.-L. Chen, A. Huang, M.-H. Ma, C.-M. Wu, W.-H. Tsai, T.-L. Hung, M.-N. Ou, H.-T. Jeng, C.-H. Lee, K.-H. Chen, W.-H. Li, M. K. Brod, G. J. Snyder, Y.-Y. Chen, *Energy Environ. Sci.* **2024**, *17*, 1904. d) T. Luo, F. Serrano-Sánchez, H. Bishara, S. Zhang, R. Bueno Villoro, J. J. Kuo, C. Felser, C. Scheu, G. J. Snyder, J. P. Best, G. Dehm, Y. Yu, D. Raabe, C. Fu, B. Gault, *Acta Mater.* **2021**, *217*, 117147; e) Z. Huang, X. Dai, Y. Yu, C. Zhou, F. Zu, *Scripta Mater.* **2016**, *118*, 19; f) H. Wu, Y. Sun, Y. Wang, H. Qin, J. Zhu, Y. Zhu, J. Hu, M. Guo, J. Liu, M. Liu, F. Guo, Q. Zhang, Z. Liu, W. Cai, J. Sui, *Mater. Today Energy* **2022**, *27*, 101045.
[11] J. Li, X. Zhang, Z. Chen, S. Lin, W. Li, J. Shen, I. T. Witting, A. Faghaninia, Y. Chen, A. Jain, L. Chen, G. J. Snyder, Y. Pei, *Joule* **2018**, *2*, 976.
[12] M. Liu, J. Zhu, B. Cui, F. Guo, Z. Liu, Y. Zhu, M. Guo, Y. Sun, Q. Zhang, Y. Zhang, W. Cai, J. Sui, *Cell Rep. Phys. Sci.* **2022**, *3*, 100902.
[13] R. Shu, Z. Han, A. Elsukova, Y. Zhu, P. Qin, F. Jiang, J. Lu, P. O. Å. Persson, J. Palisaitis, A. le Febvrier, W. Zhang, O. Cojocaru-Mirédin, Y. Yu, P. Eklund, W. Liu, *Adv. Sci.* **2022**, *9*, 2202594.
[14] a) W. D. Liu, D. Z. Wang, Q. Liu, W. Zhou, Z. Shao, Z. G. Chen, *Adv. Energy Mater.* **2020**, *10*, 2000367; b) M. Li, X. L. Shi, Z. G. Chen, *Adv. Funct. Mater.* **2024**, *34*, 2403498; c) M. Hong, M. Li, Y. Wang, X.-L. Shi, Z.-G. Chen, *Adv. Mater.* **2022**, *35*, 2208272; d) X. Zhang, Z. Bu, S. Lin, Z. Chen, W. Li, Y. Pei, *Joule* **2020**, *4*, 986; e) Y. Yu, X. Xu, M. Bosman, K. Nielsch, J. He, *Nat. Rev. Electr. Eng.* **2024**, *1*, 109; f) J. Dong, Y. Jiang, J. Liu, J. Pei, X. Y. Tan, H. Hu, A. Suwardi, N. Jia, C. Liu, Q. Zhu, Q. Yan, J.-F. Li, *Nano Energy* **2022**, *103*, 107809; g) J. Dong, F.-H. Sun, H. Tang, J. Pei, H.-L. Zhuang, H.-H. Hu, B.-P. Zhang, Y. Pan, J.-F. Li, *Energy Environ. Sci.* **2019**, *12*, 1396; h) Y. Yu, X. Xu, Y. Wang, B. Jia, S. Huang, X. Qiang, B. Zhu, P. Lin, B. Jiang, S. Liu, X. Qi, K. Pan, D. Wu, H. Lu, M. Bosman, S. J. Pennycook, L. Xie, J. He, *Nat. Commun.* **2022**, *13*, 2200124; i) Z. Guo, G. Wu, X. Tan, R. Wang, Z. Zhang, G. Wu, Q. Zhang, J. Wu, G. Q. Liu, J. Jiang, *Adv. Funct. Mater.* **2022**, *33*, 2212421; j) D.-Z. Wang, W.-D. Liu, Y. Mao, S. Li, L.-C. Yin, H. Wu, M.

Li, Y. Wang, X.-L. Shi, X. Yang, Q. Liu, Z.-G. Chen, *J. Am. Chem. Soc.* **2024**, *146*, 1681; k) Y.-F. Tsai, P.-C. Wei, L. Chang, K.-K. Wang, C.-C. Yang, Y.-C. Lai, C.-R. Hsing, C.-M. Wei, J. He, G. J. Snyder, H.-J. Wu, *Adv. Mater.* **2021**, *33*, 2005612; l) M. Samanta, K. Biswas, *J. Am. Chem. Soc.* **2017**, *139*, 9382.

[15] L. Xie, Y. Chen, R. Liu, E. Song, T. Xing, T. Deng, Q. Song, J. Liu, R. Zheng, X. Gao, S. Bai, L. Chen, *Nano Energy* **2020**, *68*, 104347.

[16] L. C. Yin, W. D. Liu, M. Li, D. Z. Wang, H. Wu, Y. Wang, L. Zhang, X. L. Shi, Q. Liu, Z. G. Chen, *Adv. Funct. Mater.* **2023**, *33*, 2301750.

[17] Y. Yu, C. Zhou, T. Ghosh, C.-F. Schön, Y. Zhou, S. Wahl, M. Raghuwanshi, P. Kerres, C. Bellin, A. Shukla, O. Cojocaru-Mirédin, M. Wuttig, *Adv. Mater.* **2023**, *35*, 2300893.

[18] a) W. Yao, Y. Zhang, T. Lyu, W. Huang, N. Huang, X. Li, C. Zhang, F. Liu, M. Wuttig, Y. Yu, M. Hong, L. Hu, *The Innovation* **2023**, *4*, 100522; b) L. Hu, B. Duan, T. Lyu, N. Lin, C. Zhang, F. Liu, J. Li, M. Wuttig, Y. Yu, *Adv. Funct. Mater.* **2023**, *33*, 2214854.

[19] D. An, S. Zhang, X. Zhai, W. Yang, R. Wu, H. Zhang, W. Fan, W. Wang, S. Chen, O. Cojocaru-Mirédin, X.-M. Zhang, M. Wuttig, Y. Yu, *Nat. Commun.* **2024**, *15*, 3177.

[20] a) M. Cagnoni, D. Führen, M. Wuttig, *Adv. Mater.* **2018**, *30*, 1801787; b) X. Zhang, J. Li, X. Wang, Z. Chen, J. Mao, Y. Chen, Y. Pei, *J. Am. Chem. Soc.* **2018**, *140*, 15883.

[21] S. Perumal, S. Roychowdhury, D. S. Negi, R. Datta, K. Biswas, *Chem. Mater.* **2015**, *27*, 7171.

[22] C. Zhang, G. Yan, Y. Wang, X. Wu, L. Hu, F. Liu, W. Ao, O. Cojocaru-Mirédin, M. Wuttig, G. J. Snyder, Y. Yu, *Adv. Energy Mater.* **2022**, *13*, 2203361.

[23] Y. Jin, D. Wang, Y. Qiu, L.-D. Zhao, *J. Mater. Chem. C* **2021**, *9*, 6484.

[24] T. Xing, Q. Song, P. Qiu, Q. Zhang, X. Xia, J. Liao, R. Liu, H. Huang, J. Yang, S. Bai, D. Ren, X. Shi, L. Chen, *Natl. Sci. Rev.* **2019**, *6*, 944.

[25] J. Li, X. Zhang, S. Lin, Z. Chen, Y. Pei, *Chem. Mater.* **2017**, *29*, 605.

[26] X. Zhang, Z. Bu, X. Shi, Z. Chen, S. Lin, B. Shan, M. Wood, A. H. Snyder, L. Chen, G. J. Snyder, Y. Pei, *Sci. Adv.* **2020**, *6*, eabc0726.

[27] a) Z. Zheng, X. Su, R. Deng, C. Stoumpos, H. Xie, W. Liu, Y. Yan, S. Hao, C. Uher, C. Wolverton, M. G. Kanatzidis, X. Tang, *J. Am. Chem. Soc.* **2018**, *140*, 2673; b) Z. Guo, Q. Zhang, H. Wang, X. Tan, F. Shi, C. Xiong, N. Man, H. Hu, G. Liu, J. Jiang, *J. Mater. Chem. A* **2020**, *8*, 21642; c) M. Hong, Y. Wang, T. Feng, Q. Sun, S. Xu, S. Matsumura, S. T. Pantelides, J. Zou, Z.-G. Chen, *J. Am. Chem. Soc.* **2019**, *141*, 1742; d) Z. Liu, J. Sun, J. Mao, H. Zhu, W. Ren, J. Zhou, Z. Wang, D. J. Singh, J. Sui, C.-W. Chu, Z. Ren, *Proc. Natl. Acad. Sci. USA* **2018**, *115*, 5332; e) M. Li, Q. Sun, S.-D. Xu, M. Hong, W.-Y. Lyu, J.-X. Liu, Y. Wang, M. Dargusch, J. Zou, Z.-G. Chen, *Adv. Mater.* **2021**, *33*, 2102575.

[28] M. Hong, Y. Wang, W. Liu, S. Matsumura, H. Wang, J. Zou, Z. G. Chen, *Adv. Energy Mater.* **2018**, *8*, 1801837.

[29] S. Perumal, M. Samanta, T. Ghosh, U. S. Shenoy, A. K. Bohra, S. Bhattacharya, A. Singh, U. V. Waghmare, K. Biswas, *Joule* **2019**, *3*, 2565.

[30] M. Hong, Z.-G. Chen, L. Yang, Y.-C. Zou, M. S. Dargusch, H. Wang, J. Zou, *Adv. Mater.* **2018**, *30*, 1705942.

[31] a) K. Biswas, J. He, I. D. Blum, C.-I. Wu, T. P. Hogan, D. N. Seidman, V. P. Dravid, M. G. Kanatzidis, *Nature* **2012**, *489*, 414; b) Z. Yin, H. Zhang, Y. Wang, Y. Wu, Y. Xing, X. Wang, X. Fang, Y. Yu, X. Guo, *Adv. Energy Mater.* **2024**, 2403174, https://doi.org/10.1002/aenm.202403174; c) Z. Yuan, M. Wu, S. Han, P. Liu, Z. Ge, B. Ge, M. Zhu, Y. Xu, W. Jie, D. Zhao, B. Yang, Y. Zhang, M. Liu, M. Zhu, C. Li, Y. Yu, C. Zhou, *Energy Environ. Sci.* **2024**, *17*, 2921; d) Y.-K. Zhu, Y. Sun, X. Dong, L. Yin, M. Liu, M. Guo, H. Wu, F. Li, Z. Guo, X. Wang, K. Yu, F. Guo, Q. Zhang, Z. Liu, W. Cai, J. Sui, *Joule* **2024**, *8*, 1; e) M. Guo, M. Liu, J. Zhu, Y. Zhu, F. Guo, W. Cai, Y. Zhang, Q. Zhang, J. Sui, *Small* **2023**, *20*, 2306251.

[32] D. An, J. Wang, J. Zhang, X. Zhai, Z. Kang, W. Fan, J. Yan, Y. Liu, L. Lu, C.-L. Jia, M. Wuttig, O. Cojocaru-Mirédin, S. Chen, W. Wang, G. J. Snyder, Y. Yu, *Energy Environ. Sci.* **2021**, *14*, 5469.

[33] a) D. Qin, H. Wu, S. Cai, J. Zhu, B. Cui, L. Yin, H. Qin, W. Shi, Y. Zhang, Q. Zhang, W. Liu, J. Cao, S. J. Pennycook, W. Cai, J. Sui, *Adv. Energy Mater.* **2019**, *9*, 1902435; b) L. You, J. Zhang, S. Pan, Y. Jiang, K. Wang, J. Yang, Y. Pei, Q. Zhu, M. T. Agne, G. J. Snyder, Z. Ren, W. Zhang, J. Luo, *Energy Environ. Sci.* **2019**, *12*, 3089; c) Y. Yu, D.-S. He, S. Zhang, O. Cojocaru-Mirédin, T. Schwarz, A. Stoffers, X.-Y. Wang, S. Zheng, B. Zhu, C. Scheu, D. Wu, J.-Q. He, M. Wuttig, Z.-Y. Huang, F.-Q. Zu, *Nano Energy* **2017**, *37*, 203.

[34] J. Zhu, X. Tan, M. Hong, Y. Wei, H. Ma, F. Feng, Y. Luo, H. Wu, Q. Sun, R. Ang, *Adv. Energy Mater.* **2024**, 2402552.

[35] J. Li, W. Li, Z. Bu, X. Wang, B. Gao, F. Xiong, Y. Chen, Y. Pei, *ACS Appl. Mater. Interfaces* **2018**, *10*, 39904.

[36] E. Nshimyimana, S. Hao, X. Su, C. Zhang, W. Liu, Y. Yan, C. Uher, C. Wolverton, M. G. Kanatzidis, X. Tang, *J. Mater. Chem. A* **2020**, *8*, 1193.

[37] a) Y. Yu, C. Zhou, S. Zhang, M. Zhu, M. Wuttig, C. Scheu, D. Raabe, G. J. Snyder, B. Gault, O. Cojocaru-Mirédin, *Mater. Today* **2020**, *32*, 260; b) Y. Yu, C. Zhou, X. Zhang, L. Abdellaoui, C. Doberstein, B. Berkels, B. Ge, G. Qiao, C. Scheu, M. Wuttig, O. Cojocaru-Mirédin, S. Zhang, *Nano Energy* **2022**, *101*, 107576.

[38] a) Y. Liu, X. Zhang, P. Nan, B. Zou, Q. Zhang, Y. Hou, S. Li, Y. Gong, Q. Liu, B. Ge, O. Cojocaru-Mirédin, Y. Yu, Y. Zhang, G. Chen, M. Wuttig, G. Tang, *Adv. Funct. Mater.* **2022**, *32*, 2209980; b) M. Liu, M. Guo, H. Lyu, Y. Lai, Y. Zhu, F. Guo, Y. Yang, K. Yu, X. Dong, Z. Liu, W. Cai, M. Wuttig, Y. Yu, J. Sui, *Nat. Commun.* **2024**, *15*, 8286; c) B. J. Kooi, M. Wuttig, *Adv. Mater.* **2020**, *32*, 1908302.

[39] a) J.-Y. Raty, M. Schumacher, P. Golub, V. L. Deringer, C. Gatti, M. Wuttig, *Adv. Mater.* **2019**, *31*, 1806280; b) L. Guarneri, S. Jakobs, A. v. Hoegen, S. Maier, M. Xu, M. Zhu, S. Wahl, C. Teichrib, Y. Zhou, O. Cojocaru-Mirédin, M. Raghuwanshi, C.-F. Schön, M. Drögeler, C. Stampfer, R. P. S. M. Lobo, A. Piarristeguy, A. Pradel, J.-Y. Raty, M. Wuttig, *Adv. Mater.* **2021**, *33*, 2102356.

[40] M. Zhu, O. Cojocaru-Mirédin, A. M. Mio, J. Keutgen, M. Küpers, Y. Yu, J.-Y. Cho, R. Dronskowski, M. Wuttig, *Adv. Mater.* **2018**, *30*, 1706735.

[41] Y. Yu, M. Cagnoni, O. Cojocaru-Mirédin, M. Wuttig, *Adv. Funct. Mater.* **2020**, *30*, 1904862.

[42] M. Wuttig, C.-F. Schön, J. Lötfering, P. Golub, C. Gatti, J.-Y. Raty, *Adv. Mater.* **2023**, *35*, 2208485.

[43] Y. Gong, W. Dou, B. Lu, X. Zhang, H. Zhu, P. Ying, Q. Zhang, Y. Liu, Y. Li, X. Huang, M. F. Iqbal, S. Zhang, D. Li, Y. Zhang, H. Wu, G. Tang, *Nat. Commun.* **2024**, *15*, 4231.

[44] J. Zhu, X. Zhang, M. Guo, J. Li, J. Hu, S. Cai, W. Cai, Y. Zhang, J. Sui, *Computat. Mater.* **2021**, *7*, 116.

[45] Y. Yu, O. Cojocaru-Mirédin, M. Wuttig, *Physica Status Solidi* **2024**, *221*, 2300425.

[46] G. J. Snyder, A. H. Snyder, M. Wood, R. Gurunathan, B. H. Snyder, C. Niu, *Adv. Mater.* **2020**, *32*, 2001537.

[47] a) M. Zhang, Z. Gao, Q. Lou, Q. Zhu, J. Wang, Z. Han, C. Fu, T. Zhu, *Adv. Funct. Mater.* **2023**, *34*, 2307864; b) Z. Liu, W. Gao, W. Zhang, N. Sato, Q. Guo, T. Mori, *Adv. Energy Mater.* **2020**, *10*, 2002588.

[48] P. Li, T. Ding, J. Li, C. Zhang, Y. Dou, Y. Li, L. Hu, F. Liu, C. Zhang, *Adv. Funct. Mater.* **2020**, *30*, 1910059.

[49] S. Chen, H. Bai, H. Wu, J. Wu, Z. Chen, X. Su, C. Uher, X. Tang, *Mater. Today Phys.* **2022**, *24*, 100682.

[50] D. G. Cahill, S. K. Watson, R. O. Pohl, *Phys. Rev. B* **1992**, *46*, 6131.

[51] J. Li, Z. Chen, X. Zhang, H. Yu, Z. Wu, H. Xie, Y. Chen, Y. Pei, *Adv. Sci.* **2017**, *4*, 1700341.

[52] J. Li, X. Zhang, X. Wang, Z. Bu, L. Zheng, B. Zhou, F. Xiong, Y. Chen, Y. Pei, *J. Am. Chem. Soc.* **2018**, *140*, 16190.

[53] a) Y. Gelbstein, J. Davidow, S. N. Girard, D. Y. Chung, M. Kanatzidis, *Adv. Energy Mater.* **2013**, *3*, 815; b) P.-Y. Deng, H.-J. Wu, *A.C.S. Appl. Energy Mater.* **2022**, *5*, 9031.

[54] J.-Y. Raty, M. Wuttig, *J. Phys. D: Appl. Phys.* **2020**, *53*, 234002.